Step-by-Step Validation of Antarctic ASI AMSR-E Sea-Ice Concentrations by MODIS and an Aerial Image

Qian Shi, Jie Su, Georg Heygster, *Member, IEEE*, Jiuxin Shi, Lianzhong Wang, Lizhong Zhu, Quanli Lou, and Valentin Ludwig

Abstract— The lack of *in situ* data has always posed challenges to remote-sensing-data product validation. Herein, the products of sea-ice concentration (SIC) data derived using the arctic radiation and turbulence interaction study (ARTIST) sea ice (ASI) algorithm were evaluated by comparing them with SICs from a high-resolution sea-ice aerial image obtained during the 27th China Antarctic expedition in January 2011. Results suggest that data obtained from the advanced microwave scanning radiometer for the earth-observing system (AMSR-E) underestimate SICs by 19%. We performed step-by-step comparisons among the aerial image, moderate-resolution-imaging spectroradiometer (MODIS), and AMSR-E SIC. These types of comparisons have not been made in previous validation studies. First, SICs acquired from MODIS-Terra imagery were acquired using a tie-point method and corrected by SICs derived from the aerial photography. Second, SICs of MODIS-Aqua images were trained based on the consistency of SIC results between MODIS-Terra and MODIS-Aqua over the selected region on the same day. Finally, the MODIS-Aqua SICs were employed to validate synchronous AMSR-E swath SIC products. The results show that the AMSR-E products underestimate SICs by 8.5% in the marginal ice zone in comparison with MODIS SICs. According to our further analysis between sea-ice types and AMSR-E biases, the higher the proportion of first-year ice, the smaller the AMSR-E SIC bias. In other words, results suggest that the higher the thin ice proportion, the more the AMSR-E underestimates the SIC.

Index Terms— Aerial imagery, AMSR-E (advanced microwave scanning radiometer for the earth-observing system) data, step-by-step validation, sea-ice concentration (SIC).

I. Introduction

SATELLITE remote-sensing data have become a crucial means of polar-climate observation since 1979 [1], [2]. Sea-ice concentration (SIC), which is defined as the ratio of the ice-covered area to the total area, is a parameter of primary interest. The accuracy of remote-sensing SIC data sets is essential for the modeling processes involved in the interaction between ocean and atmosphere in numerical weather prediction and for data assimilation [3], [4].

Owing to the limited influence of cloud cover, independence from daylight, and temporal continuity, passive-microwave data have been significant for investigating SICs in polar regions. Currently, the most widely used SIC data products are those based on data acquired by the NASA Team (NT) and Bootstrap algorithms (BT) [5], [6]. Both use the Nimbus-7 SMMR and DMSP SSM/I-SSMIS 19- and 37-GHz brightness temperature (TB) measurements, with a nominal spatial resolution of 25 km. The higher resolution advanced microwave scanning radiometer for the earth-observing system (AMSR-E) was in operation from 2002 to 2011, and an enhanced NT SIC algorithm has been developed for it [7]. At present, the advanced microwave scanning radiometer (AMSR2), which is the successor sensor of AMSR-E, is operating and distributing SIC products by the same ASI algorithm as AMSR-E. Also, the ocean and sea ice satellite application facility (OSISAF) of the European Organization for the Exploitation of Meteorological Satellites proposed a hybrid algorithm that takes advantage of the Bristol algorithm [8] in low-SIC regions and the BT algorithm in high-SIC regions [9].

Previous studies have evaluated the abovementioned SICs using different kinds of measurements and acquired valuable knowledge for these SIC products. In general, all four algorithms perform better in winter than in summer and could capture the SIC in pack ice better than in marginal ice zones [10]–[17]. The BT SICs are higher than NT SICs, and the hybrid OSISAF algorithm usually has the lowest bias. The differences in SICs between passive-microwave retrieval and SIC from higher resolution measurements, such as visible light sensors and aerial images, mainly result from atmospheric water-vapor content and ice-surface melting processes in the Arctic [12]–[15]. In the Antarctic, ice-flooding processes due to the distinctive thick snow layer also contribute to the SIC bias [18].

The AMSR-E SICs released by the University of Bremen and discussed herein were based on the Arctic radiation and turbulence interaction study (ARTIST) sea ice (ASI) algorithm [19], [20]. Due to the use of 89-GHz TBs, the SICs based on this algorithm have a spatial resolution of 6.25 km, which is double that of the 19- and 37-GHz TBs used by the NT and BT

Qian Shi, Jie Su, and Jiuxin Shi are with the Key Laboratory of Physical Oceanography, Ocean University of China, Qingdao 266100, China, and also with the Qingdao National Laboratory for Marine Science and Technology, Qingdao 266100, China (e-mail: sujie@ouc.edu.cn).

Georg Heygster and Valentin Ludwig are with the Institute of Environmental Physics, University of Bremen, 28359 Bremen, Germany (e-mail: heygster@uni-bremen.de).

Lianzhong Wang, Lizhong Zhu, and Quanli Lou are with the Heilongjiang Administration of Surveying, Mapping and Geoinformation, Harbin, China.

Color versions of one or more of the figures in this article are available online at https://ieeexplore.ieee.org.

Digital Object Identifier 10.1109/TGRS.2020.2989037

algorithm. Compared with previous coarse passive-microwave SIC products, AMSR2 ASI SICs capture the ice edge more accurately [21]. Due to the similar sensor configurations and the same retrieval algorithm between AMSR-E and AMSR2, the AMSR-E ASI SICs are deemed to have better performance in the marginal ice zone than other passive-microwave SICs with lower resolutions. However, the ASI algorithm is more sensitive to atmospheric effects, and it typically overestimates SICs in winter and underestimates SICs in summer in the marginal ice zone. The underestimation was -13.6% based on ship observations [22] and was -8.9% based on visible images [23], [24]. Also, further studies indicate that ice-surface processes, such as abnormal ice temperature and snow metamorphism, contribute to the ASI SIC bias [25], [26].

Apart from high-resolution satellite visible and synthetic-aperture radar imagery, aerial imagery is a proven means for observing sea ice and validating passive-microwave-based retrievals. Compared with the SICs derived from aerial images during the Third China Arctic Expedition, ASI overestimates the SIC by $14\% \pm 9\%$ when the SIC is greater than 80% [27]. The footprints of aerial images are smaller than passive-microwave images, and this inconsistency results in additional uncertainties remaining in the verification results.

In summary, previous assessments have already revealed the limitations of the ASI-based SIC. However, time-lapse and ground-coverage differences across sensors weaken the reliability of those assessments. The proposed study aims to verify the swath AMSR-E ASI-based SICs from the University of Bremen using imagery from the moderate-resolution imaging spectroradiometer (MODIS) and an aerial image. Sea ice concentration from AMSR2 will not be discussed in this article because the aerial field campaign occurred during the operation of AMSR-E. We applied a step-by-step validation by introducing the coincident MODIS-Aqua image to assess the swath AMSR-E SICs derived from the ASI algorithm. We first used the SICs based on the aerial image to validate the MODIS SICs, which we then compared with the AMSR-E SICs.

This article is presented herein as follows. In Section II, we introduce the sources of data and the inversions of different kinds of raw data. In Section III, we first directly assess the SIC derived from AMSR-E SIC by SIC derived from the aerial image. Second, the aerial image SICs are used to train the tie-points of the pixel-based MODIS-Terra SIC algorithm, which is then used for determining the tie-points of the subsequent MODIS-Aqua data. Then, we validate the SICs from AMSR-E swath data by synchronous MODIS-Aqua SIC data and investigate the relation between the underestimation of SIC and the ice types using the broadband-albedo derived from land surface reflectance in three visible spectra. In Section IV, we give possible reasons for the AMSR-E SIC bias, and in Section V, we summarize our work and examine the future of validation work.

II. Data Sources and Preprocessing

A. Aerial Image

The investigation area is marginal to the Amery Ice Shelf, bordering the Prydz Basin (Fig. 1). During China's 27th
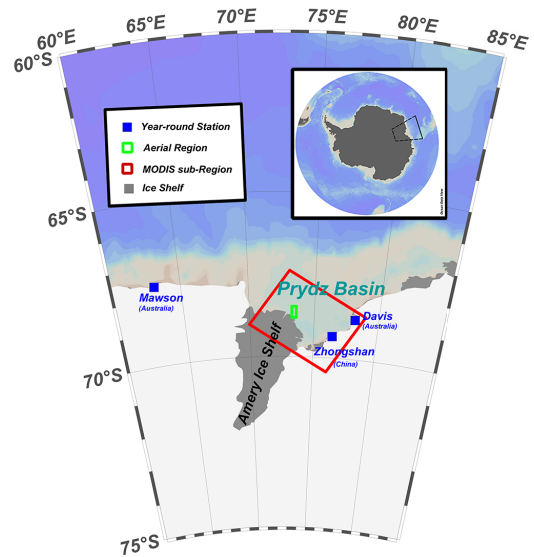

Fig. 1. Locations of the aerial image (the green outlined area) and MODIS-terra subimagery (the red outlined area). The white and gray areas represent ice sheet, and ice shelf, respectively.

Antarctic Expedition, scientists conducted an airborne sea-ice survey and took aerial photographs of this area. The aerial survey started at 2:40 UTC on January 9, 2011, lasting 3.5 h with a helicopter flying more than 30–24-km-long survey lines along the meridian. The average flight altitude of the helicopter was 800 m, and the mean flight speed was 140 km/h. The digital camera used for aerial photography was installed under the helicopter. This campaign yielded 30 transects for a total of about 100 images of 5440×4080 pixels each. The distance between adjacent images is 240 m, and the overlap ratio is about 65%. The spatial resolution of the composite image [Fig. 2(a)] is about 3.82 m, covering an area of 526 km^2. The composite image was geolocated based on three fixed points located on the ice shelf. The position error was determined from a GPS device to be <1 m. See [28] for detailed information on campaign observations and geolocation calibration of the composite aerial image. To readily compare them with other data, the aerial image was mapped into a polar stereographic grid before assessment.

B. MODIS Data

The polar-orbiting satellites Terra and Aqua were launched in 1999 and 2002, respectively. Each carries a MODIS sensor, herein referred to as MODIS-Terra and MODIS-Aqua with 36 channels (250-, 500-, and 1000-m spatial resolution). Terra and Aqua have sun-synchronous orbits with equator crossings at 10:30 A.M. and 1:30 P.M., respectively. Both MODIS-Aqua and AMSR-E are on the same satellite, making MODIS-Aqua an optimal tool for validating AMSR-E data products. The MODIS-Terra is nearly synchronous with the aerial image, whereas the MODIS-Aqua is strictly synchronous with AMSR-E. We used both kinds of MODIS imagery for connecting the high-resolution aerial image and the coarser AMSR-E data.

The MODIS bands used for retrieving SIC are Level 2 (MOD02) red (0.620–0.670 μm), green (0.545–0.565 μm),
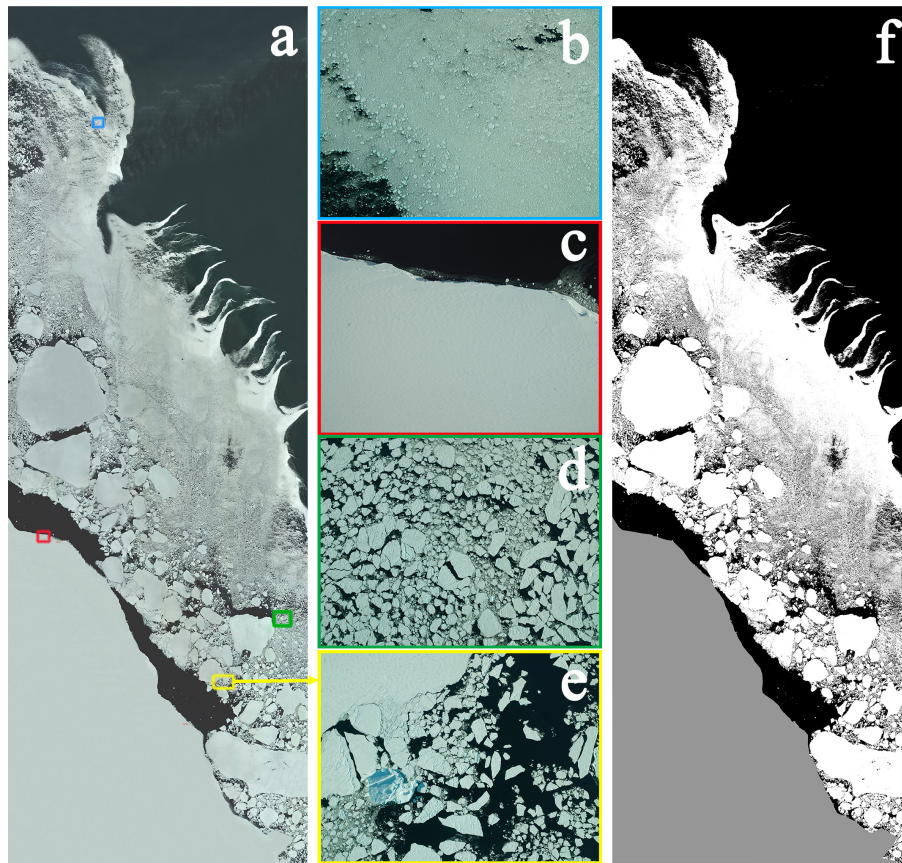
Fig. 2. Mosaicked aerial image, acquired on January 9, 2011. (a) Total area of the aerial image. Subregions dominated by (b) brash ice; (c) ice shelf; (d) ice floes; and (e) float ice with a small iceberg. (f) Ice–water binary image after threshold discrimination corresponding to (a), in which black/white/gray pixels represent open water/sea ice/ice shelf, respectively.

and blue (0.459–0.479 μm) top of atmospheric radiance (∼500-m spatial resolution) from NASA [29]. The MODIS images were projected into a polar stereographic grid before assessment.

True-color MODIS-Terra image composites of bands (1–4–3) reflectance, covering the area marginal to the Amery Ice Shelf (bordering the Prydz Basin) on January 9, 2011, are shown in Fig. 3. Based on the visible image, we know that the sky was clear in the daytime, except for minor thin clouds (not shown) just before noon. West of the aerial field (the green rectangle), there was a field of brash ice, and the region east of it was full of pack ice and fast ice.

The MODIS radiance was converted into land surface reflectance using Fast Line-of-sight Atmospheric Analysis of Spectral Hypercubes (FLAASH) atmospheric correction model based on the MODTRAN4 radiation transfer code in the ENVI software [30]. The atmospheric correction method used in this article is consistent with the one used in Su and Wang [31], and the detailed information could be referred to there. The solar zenith for MODIS-Terra scan at 03:25 is 57° and is 50°, 56°, and 88° for MODIS-Aqua scans at 09:05, 10:40 and 18:45, respectively.

The MODIS-Terra scan was acquired at 03:25, January 11, 2011, and could be considered to be synchronous with the aerial image started at 02:40. The acquisition time of three MODIS-Aqua scans on the same day is 09:05, 10:40, and 18:45, respectively.
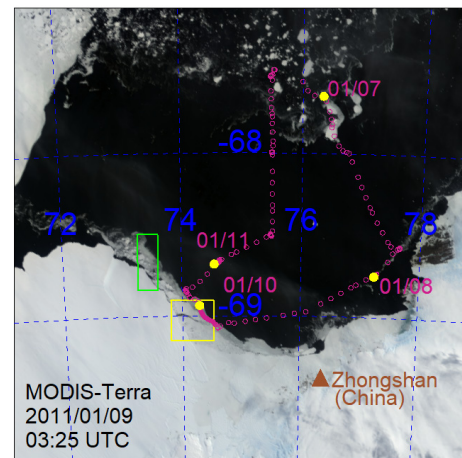

Fig. 3. True-color composite image of top of atmospheric reflectance in red band 1 (0.620–0.670 μm), green band 4 (0.545–0.565 μm), and blue band 3 (0.459–0.479 μm) acquired by MODIS-Terra at 03:25 UTC, January 9, 2011. The green outline (rectangle) corresponds to the aerial image [Fig. 2(a)]; the yellow outline (square), to quasimotionless area (Fig. 9); the violet red circles, to tracers of R/V *Xuelong*; and the colored dots, to positions during the aerial observation (initial positions during January 7–11 are shown in yellow).

C. AMSR-E SIC

Daily AMSR-E SIC products from the University of Bremen [19], [20], which we validated in this article, were provided using the standard Polar Stereographic Grid (6.25-km spatial resolution) Fig. 4(a) and (b)]. The ASI algorithm
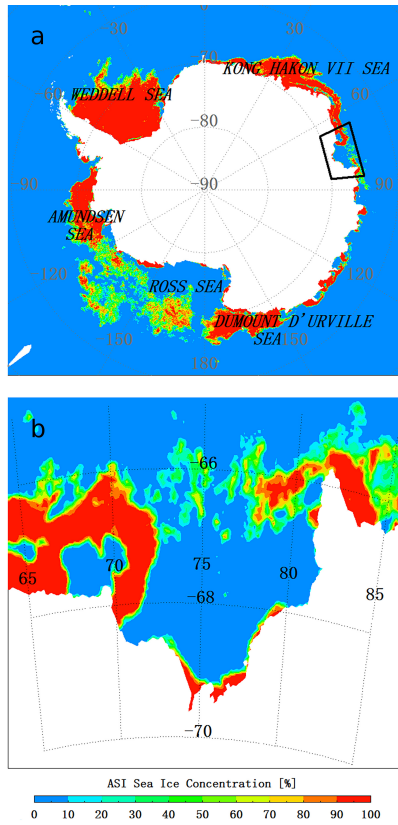
Fig. 4. (a) Antarctic SIC January 9, 2011, based on using the ASI algorithm. (b) SIC of Amery Ice Shelf corresponding to the black outline (the quadrilateral) in Fig. 4(a). Data were produced from daily AMSR-E by Bremen University.
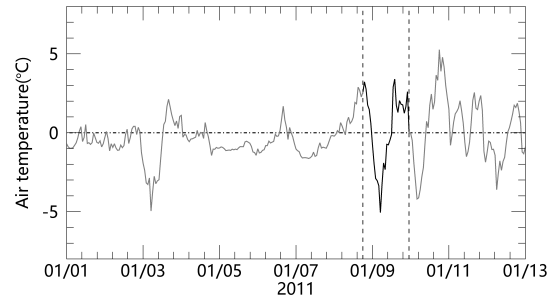

Fig. 5. Air temperature from cruise observation onboard R/V *Xuelong*. Time series between vertical dashed lines started at 18:00 UTC on January 8, 2011, and ended at 23:00 UTC on January 9, when vessel was in pack ice ~50 km from area of the aerial campaign.

D. Thin Ice Thickness

Thin ice is semitransparent in microwave bands so that the emission from the water below the ice also contributes to the microwave signal [15]–[17]. This effect is only pronounced at low microwave frequencies and is used to detect the thickness of thin ice. For this article, data on the thickness of thin sea ice in the Antarctic was acquired from the University of Bremen Data Center. The data had been retrieved from the L-band microwave Soil Moisture and Ocean Salinity sensor (SMOS). The retrieval algorithm is based on the relation between polarization differences and intensity of TB [32], [33].

E. Meteorological Observation Onboard R/V Xuelong

Hourly air-temperature data were recorded on VAISALA MILOS 500 Data Collection and Processing System onboard R/V *Xuelong* during the period of the aerial observation, which was occurring about 50 km away from the vessel [34]. Based on the weather records, there was a cooling process during the aerial campaign period in January 2011 (Fig. 5).

III. STEP-BY-STEP VALIDATION

In this section, we will first compare AMSR-E SIC by aerial image SIC directly. There are many surface types in Prydz Bay, including ice sheets, ice shelf, fast ice, pack ice, polynya, and open water, making this region an ideal experimental place for the validation of microwave remote-sensing products. The ice shelf in this area can also provide a natural reference for the geolocation of the aerial image and satellite remote-sensing data, which ensures the geographical consistency of different data sources. The aerial coverage focused on the leading edge of the Amery Ice Shelf [Fig. 2(a)]. In contrast to the shelf ice, sea ice in the Antarctic was melting during the research period. We could recognize the mixture of brash first-year and flat first-year ice with snow cover (after enlarging) from Fig. 2(d) and (e).

The technique of step-by-step validation applied herein uses data sources at different resolutions: aerial image (3 m), visible imagery (500 m), and the passive-microwave data (6.25 km). First, the SIC values obtained from the aerial image were used to validate the MODIS SICs, and then the thus-proven MODIS SICs were compared with the AMSR-E microwave SIC products. One of the prerequisites for the step-by-step

determines the SIC based on a third-order polynomial of the polarization difference of the 89-GHz v-pol and h-pol channels, which have the highest resolution among the channels of the instrument. This nonlinearity serves to account statistically for the atmospheric influence on the microwave signal. In addition, three "weather filters," based on the 18- and 37-GHz channels, screen out spurious ice concentration generated incorrectly by the algorithm in open water regions of high atmospheric water vapor and cloud liquid water. Fig. 4 gives the SIC distribution of the Antarctic Ocean and the region near Amery Ice Shelf.

According to Fig. 4, on January 9, 2011, Weddell Sea, Amundson Sea, King Haakon VII Sea, and Dumount D'Urville Sea were still covered by the dense sea ice, but the sea ice had already melted in the Ross Sea and Prydz Bay, resulting in a large area of open water. West of 75° E, along the Amery Ice Shelf from northwest to southeast, pack ice got denser. We noticed that in the ASI SIC product [Fig. 4(b)], part of the shelf ice (74° E–75° E, 69.3° S–69.6° S) extending into the Amery Ice Shelf is incorrectly considered to be 100% sea ice.

We excluded these data before assessing the passive-microwave SIC accuracy. Furthermore, in order to avoid the influence on AMSR-E SIC validation resulting from the ice drift, we employed the swath AMSR-E SICs instead of the daily mean AMSR-E SICs were employed when comparing with the MODIS-Aqua data.

verification is the quasisynchronization of the different data sources. The acquisition time of the composite aerial image was 02:40–06:10 UTC. During this period, there were two MODIS-Terra transits at 03:25 UTC and 05:05 UTC, respectively. The first one had better spatial consistency with the composite aerial image. Therefore, as the first step, we compared the composite aerial image SICs with MODIS-Terra data at 03:25 UTC to determine the tie points of sea ice and open water for the MODIS-Terra SICs retrieval algorithm, and then we calculated the MODIS-Terra SICs. Next, in the second step, a quasimotionless area was selected to accomplish SICs comparison between MODIS-Aqua and MODIS-Terra. The SICs inversion parameters of MODIS-Aqua imagery were thus determined. Finally, the MODIS-Aqua SIC results were used to validate the swath AMSR-E SICs, as the MODIS-Aqua and AMSR-E are on the same satellite.

A. Deriving SICs From the Composite Aerial Image

A prerequisite for accurately extracting SICs is distinguishing sea ice from open water correctly in the aerial image. As shown in the composite aerial image [Fig. 2(a)], the ice shelf is in the southwest, and floating ice circulates along the edge of the ice shelf in a roughly northwest–southeast direction. Open water covers the northeast part of the region. The study area contains regions of brash ice [Fig. 2(b)], ice shelf [Fig. 2(c)], pack ice [Fig. 2(d)], and small icebergs [Fig. 2(e)]. The optical properties of the ice shelf are close to those of thick ice with dry snow and are brighter than typical pack ice in the summertime. If the shelf ice is classified as sea ice, some darker pack ice will be interpreted as open water, resulting in an underestimation of SIC in the aerial image. As a consequence, we first constructed an ice-shelf mask using the Environment for Visualizing Images (ENVI) geospatial software, and then, after removing the influence of the ice shelf, distinguished the sea ice from open water in the image.

We used a MINERROR threshold algorithm to distinguish sea ice and open water [35]. The discriminant algorithm assumes that the gray value (0–255) histogram of the image obeys a bimodal Gaussian distribution. At the selected threshold, the cost function based on a Bayesian classification reaches its minimum. The thresholds that we found for the three components of the true-color composite aerial image were 118, 141, and 140. In the binary image, the pixels with all three channels greater than the corresponding threshold were labeled as ice, whereas the remaining pixels were labeled as water. The classification results in Fig. 2(f) effectively distinguish the characteristics of brash ice and recognize the pixels that have high reflectance among open waters [upper right in Fig. 2(a)] reasonably well. Accordingly, they demonstrate the reliability of the aerial image SICs.

After projecting the discriminated aerial binary image onto the MODIS (500-m) and AMSR-E (6.25-km) polar stereographic grids, we counted the number of the aerial ice pixels in each of the two kinds of grids and calculated the SICs. Then, we used the results to verify the AMSR-E SICs (Section III-B) and to determine the MODIS-Terra SICs (Section III-C).
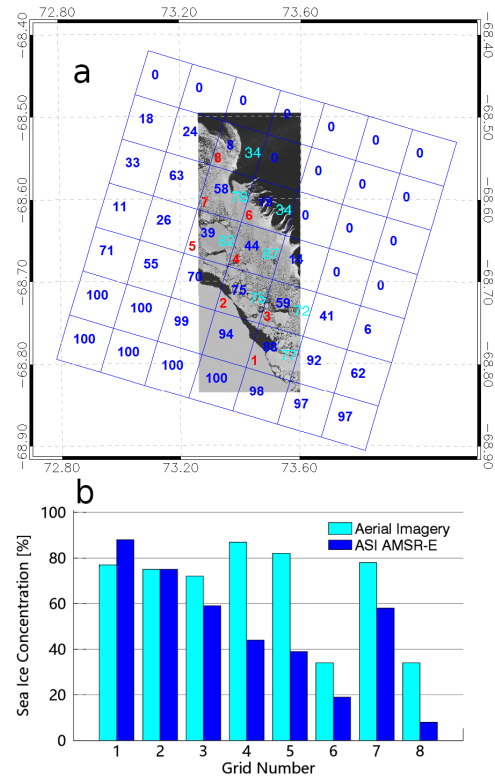

Fig. 6. (a) Sea ice concentration distribution in the polar grid based on data acquired by the mosaicked aerial image (cyan numbers) and AMSR-E (blue numbers). Red numbers (ranging 1–8) denote grid serial numbers. (b) Blue bars denote SIC (%) versus grid serial number; cyan bars, area-averaged SIC.

B. Validation of AMSR-E SICs With the Aerial Image SICs

The aerial image SICs on the AMSR-E grids are presented in Fig. 6 as cyan numbers. Only the AMSR-E grids with aerial campaign coverage exceeding 70% were calculated. Visually, the ASI results appear plausible. We performed a point-by-point comparison between the aerial image SICs and ASI AMSR-E SICs (Fig. 6(a), the blue numbers): grid cells 1 and 2 (the red numbers) are dominated by flat first-year ice with snow cover; grid cells 3–5 by mixed pack ice and brash ice; and grids 6–8 by low-brightness brash ice.

The results show that the ASI SICs in the sea ice covered area (grids 1–8) are on average 19% lower than the aerial image SICs, and the root mean square (rms) error is also 19%. In the region near the ice shelf (grids 1 and 2), the average AMSR-E SIC is 76% and the mean bias is 5.5%. In grids 3–5, the average AMSR-E SIC is 80% and the mean bias is −33%. In the marginal ice zone (grids 6–8), the average AMSR-E SIC is 49% and the mean bias is −20%. We also noted that the strongest underestimation (−43%) did not appear near the edge of the ice but in the region with high SIC, so this phenomenon is worth further investigation.

C. Retrieval of MODIS-Terra SIC by Calibrated Tie Points Using the Aerial Image SIC

Although the aerial image is a valuable means for verification of the AMSR-E SIC product (Section III-B), such an image may yield only eight AMSR-E grid cells. The time

TABLE I
ALBEDO TIE POINTS OF FOUR MODIS-AQUA
GRANULES ON JANUARY 9, 2011

Transit time (UTC)	A_w	A_I
09:05	0.06	0.67
10:40	0.08	0.67

gap between the aerial image and daily AMSR-E product may thwart error analysis. However, MODIS-Aqua, due to its broad spatial coverage and synchronization with AMSR-E, can make up for these deficiencies.

The threshold method represents a conventional means for distinguishing sea ice and open water in visible-imagery datasets [36]. However, this method cannot resolve more-detailed, within-pixel ice information. Currently, threshold methods, also called *tie-point methods*, are widely used to extract ice concentration from visible imagery [37]–[40]. The selection of ice/open water tie-points is influenced by the solar zenith angle, atmospheric water-vapor content, and sea-ice microphysical properties. Therefore, different visible images should use different tie points for retrieving SICs. Key *et al.* [39] and Liu *et al.* [40] proposed determining local tie points for each pixel based on the visible images without external data sources and achieved good results with data of the Visible Infrared Imaging Radiometer Suite (VIIRS). However, due to using such a high-resolution aerial image, we determined uniform tie points of ice and water of MODIS imagery based on the aerial image.

MODIS-Terra SIC retrieval was performed as follows. First, we calculated broadband albedo (BBA) [41]

$$\alpha = R1 \times 0.3265 + R4 \times 0.2366 + R3 \times 0.4364 \quad (1)$$

where R_1, R_4, and R_3 represent surface reflectance in bands red, green, and blue, respectively. The MODIS L2land surface reflectance was divided by the cosine of the solar zenith angle (Table I) to correct for the atmospheric path length [41].

Then, the MODIS SIC was calculated by the tie-point method

$$SIC = \frac{\alpha - A_W}{A_I - A_W}. \quad (2)$$

The histogram of MODIS-Terra BBAs [Fig. 7(a), corresponding to Fig. 3)] shows the main peak near 0.051 with a smaller peak near 0.021. The smaller peak is interpreted as open water under clear sky conditions. The higher BBA values representing sea ice have a much broader distribution, with two peaks an order of magnitude smaller than the main peak. They are interpreted as thin ice (BBA = 0.55) and thick first-year ice with snow cover (BBA = 0.755), after the masking of ice-shelf pixels [Fig. 7(a)].

To accurately determine the tie points of open water (A_W) and ice (A_I) used for MODIS-Terra SIC retrieval, we refer to the aerial image SICs (Section III-A) as ground truth to measure the spatially averaged absolute bias of SICs between the aerial image and MODIS-Terra imagery. We select the tie-points for further MODIS-Terra SIC retrieval when absolute bias reaches the minimum. Since the BBA of
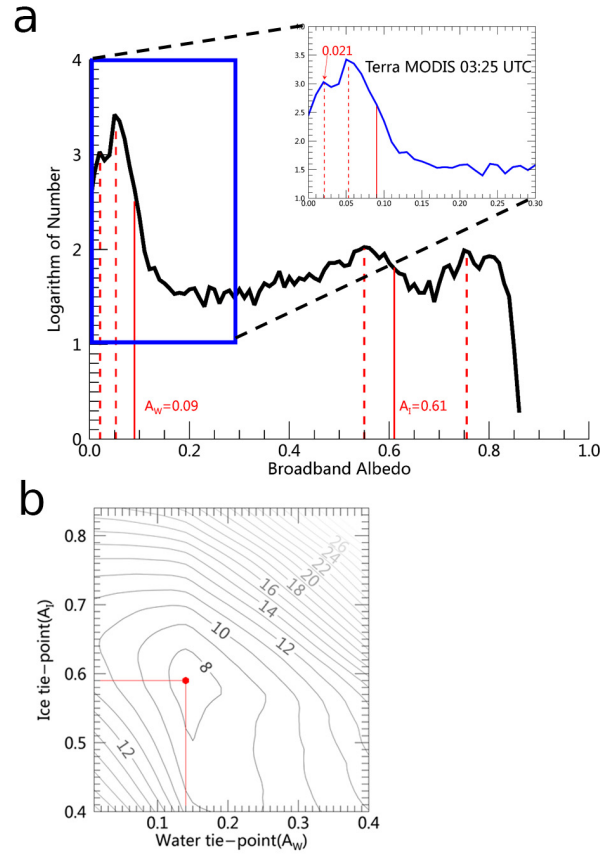

Fig. 7. (a) Logarithmic histogram of broadband albedo (BBA) detected by MODIS-Terra at 03:25 UTC, January 9, 2011. The red dashed lines indicate BBA peaks discussed in Section III-C. (b) Average absolute bias between two SIC data sets obtained from MODIS-Terra and the aerial image versus the different pairs of ice and water tie points, A_W and A_I.

seawater is <0.4 and BBA of ice is mostly >0.4, we assumed A_W to be in the range 0.01–0.40 and A_I to be between 0.41 to 0.85 with an interval of 0.01, and then obtained the corresponding MODIS-Terra SIC values. When calculating the SIC bias, the aerial image was divided into 5×15 subregions, including approximately 654×654 aerial image pixels and 5×5 MODIS-Terra pixels per subregion after projection onto the polar stereographic grid. SIC for each subregion was calculated by the spatially averaged SICs over each subregion. In Fig. 7(b), the average SICs bias of MODIS and the aerial image reaches a minimum at $A_w = 0.14$ and $A_I = 0.59$ [red dots in Fig. 7(b)]. Based on (2), using these tie points, the SICs of the MODIS-Terra (Fig. 8) represent the ice edge and leads in the marginal zone as well as the brash ice in the northwestern part (Fig. 3).

D. Retrieval of MODIS-Aqua SIC by Calibrated Tie Points Using MODIS-Terra SIC

The time lag between the MODIS-Terra and the AMSR-E data is more than 5 h, while the MODIS-Aqua scenes in Fig. 9 are synchronous with the AMSR-E data. Therefore, in the second place, and taking into account the minimum SICs difference between the MODIS-Terra and MODIS-Aqua, we determined A_W and A_I of the MODIS-Aqua SIC retrieval algorithm and calculated the MODIS-Aqua SICs.
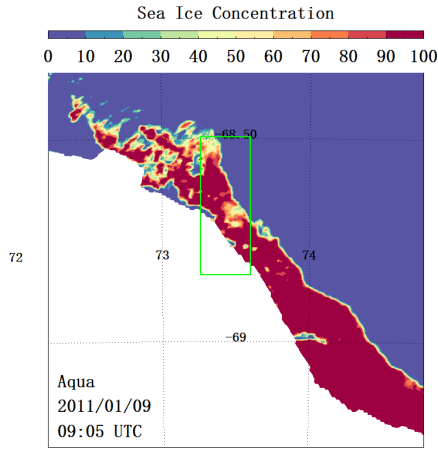
Fig. 8.   MODIS-Terra SIC covering Amery Ice Shelf calibrated by the aerial image on January 9, 2011 (UTC). Green rectangles correspond to the aerial-image region in Fig. 2(a) and the white pixels represents Amery Ice Shelf.
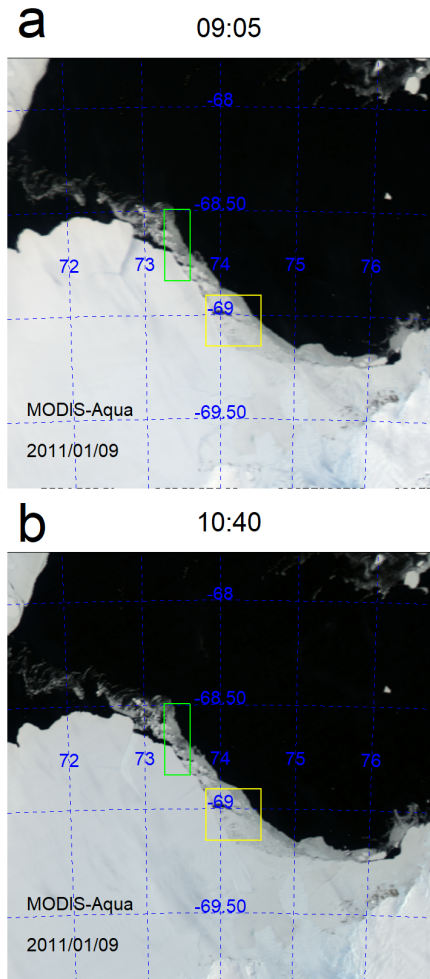

Fig. 9.   True-color (composited bands 1–4–3) images from MODIS-Aqua covering Amery Ice Shelf at two transit times on January 9, 2011. Overflight times were (a) 9:05 and (b) 10:40 UTC; the green rectangles correspond to the aerial image region in Fig. 2(a); and the yellow rectangles represent quasimotionless area used to determine tie points for MODIS-Aqua images.

After comparing Figs. 3 and 9, we found that the pack ice has drifted during the time gap between the MODIS-Terra and MODIS-Aqua. By manual feature tracking of the floes,
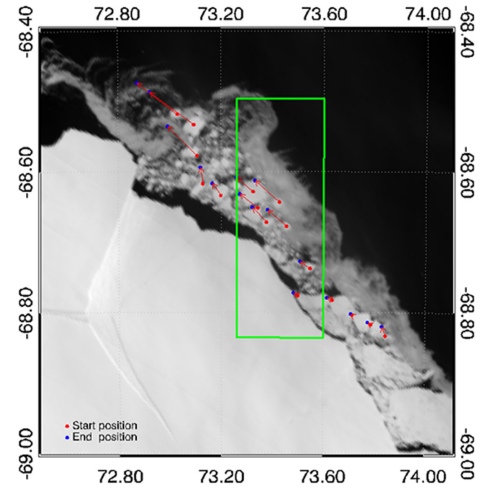

Fig. 10.   Sea-ice displacement vectors (red arrows) derived from MODIS-Terra and MODIS-Aqua 250-m reflectance on January 9, 2011, based on features recognized manually. The red and blue dots represent start and end points of displacement extraction, respectively. The green rectangle corresponds to the aerial image in Fig. 2(a).
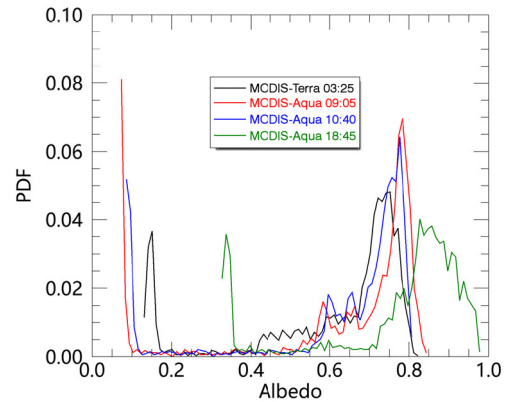

Fig. 11.   Histograms of broadband albedo detected by MODIS-Terra and MODIS-Aqua overflights on January 9, 2011, in quasimotionless sea-ice area (Figs. 3 and 9). [probability density function (PDF)].

we determined the MODIS sea-ice drift vectors (Fig. 10). The average ice speed was 11.9 cm/s in the northwest direction along the shelf-ice edge. However, there was a velocity shear between brash ice and pack ice, so we could not get MODIS-Aqua SICs just by translating MODIS-Terra SICs. Nonetheless, we found the quasimotionless area (the yellow outlined region in Fig. 3) barely changed between one MODIS-Terra scene and three MODIS-Aqua scenes on the same day. This allowed us to use the MODIS-Terra SICs in that area to determine the tie points of two MODIS-Aqua scenes (Fig. 9).

After the solar-zenith-angle correction (Section III-B), we obtained the BBAs of the four MODIS images (Fig. 11). For the three MODIS-Aqua images taken at different times (Table I), there were significant peaks for all BBA histograms corresponding to open water, sea ice, and ice-shelf ice from left to right. The curves plotted from MODIS-Aqua scenes are similar to those from MODIS-Terra. However, the scene at 18:45 was excluded because the corresponding AMSR-E observations do not cover the study region (AMSR-E has narrower swath width than MODIS).
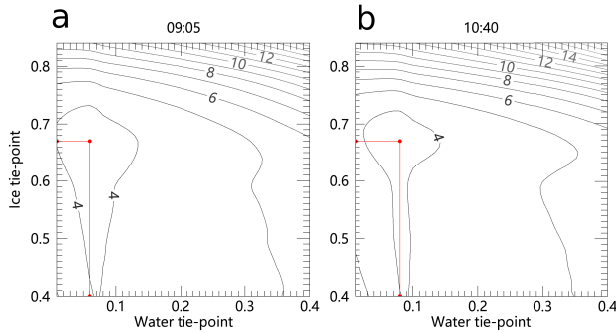
Fig. 12. Contours of average absolute bias between SIC obtained from MODIS-Aqua and MODIS-Terra. Data shown are for two MODIS-Aqua overflights, (a) 9:05 UTC and (b) 10:40 UTC, and for MODIS-Terra using different pairs of tie points A_W and A_I. The red lines indicate selected values for A_W and A_I used in SIC-retrieval algorithm for two MODIS-Aqua overflights.

Using the method of determining tie points for MODIS-Terra imagery, we studied the variation of the average absolute bias between MODIS-Terra and MODIS-Aqua images with different pairs of tie points by varying them in steps of 0.01 [Fig. 12(a) and (b)]. We chose to locate A_W and A_I to be where the average absolute bias reaches the minimum. Afterward, we calculated the SIC values of the corresponding MODIS-Aqua images based on the chosen pairs of A_W and A_I (Table I).

E. Comparison Between MODIS and AMSR-E SICs

We projected the obtained MODIS-Aqua SICs (Section III-D) into the AMSR-E 6.25-km polar stereographic grid, averaged over the grid cells, and compared with swath ASI SIC products from the University of Bremen. According to Fig. 13, AMSR-E SICs are consistent with MODIS-Aqua SICs near the ice shelf and open water, but they underestimate the SICs of all the sea-ice grids. The average SIC underestimation is 8.5% after removing the ice shelf. The underestimation mainly resulted from the regions with SIC lower than 70%, which are close to the open water [pixels with red numbers in Fig. 13(b)]. We maintain that this underestimation mainly originates from the strong water signal in these regions characterized by much brash ice.

IV. DISCUSSION

The aerial campaign was performed under clear sky conditions. However, the MODIS imageries are acquired at a higher altitude and are more sensitive to the clouds. Even though the atmospheric corrections have been conducted before acquiring MODIS land surface reflectance, the atmospheric correction could not exclude the influence of clouds. We have examined the MODIS cloud mask derived from the MOD35 data set [42] and found the study area to be generally clear (not shown here) in the MODIS imageries. Consequently, we are more confident about the MODIS evaluation results.

Previous studies argued that the underestimation of ASI SIC in low-SIC regions mainly results from thin ice or newly formed ice [15]–[17]. Sea-ice flooding caused by thick snow is

another reason for passive-microwave SIC underestimation in the Antarctic [18]. In general, sea ice was melting during the study period, and we could not associate the underestimation of ASI SIC with new ice intuitively. Moreover, the albedos for pixels where ASI underestimates SICs were not high enough to be recognized as sea ice covered by thick snow, so we could start with a preliminary exclusion of the sea ice flooding process when studying the SIC underestimation. Using only the albedo of visible imagery, we could not acquire detailed information about sea-ice, such as ice thickness and ice evolution. As a result, we further analyzed the ASI SIC underestimation by considering ice type and ice thickness.

Following the work of Cavalieri *et al.* [18] and using the World Meteorological Organization nomenclature [43], we classified sea ice on the basis of BBA from MODIS-Aqua imagery. However, what Cavalieri *et al.* [18] labeled as "new ice" referring to ice with the lowest albedo, we conservatively call it "thin ice" since empirically, sea ice was melting rather than growing during the study period. As a result, we classified this sea ice into thin ice and first-year ice. Additionally, the albedo thresholds they used, which are suitable for the ice at the surface in October, may not be as such for our study. Accordingly, for the most part, we used the albedo thresholds of ice types from Brandt *et al.* [44] based on *in situ* observations of Antarctic sea ice. The threshold of open water we used is 0.04 larger than that used by Brandt *et al.* [44] (0.08), so that the small leads in the ice can be detected more clearly. We used the following classification criteria for the four surface types:

1) open water: BBA < 0.12;
2) thin ice: $0.12 \leq$ BBA < 0.71;
3) first-year ice: BBA ≥ 0.71.

According to these thresholds, all MODIS ice pixels were classified as either thin ice or first-year ice [corresponding to the blue and red dots in Fig. 14(a)]. East of the aerial survey region (the green rectangle), in the direction from the ice shelf toward open water, the classification results show an orderly progression from first-year ice to thin ice. An ice-thickness dataset has also provided evidence that thin ice indeed exist in the study region. Based on the measurements of thin-ice thickness from the SMOS [34], [35] (Fig. 15), the study region was covered by relatively thin sea ice (maximum <45 cm thick). According to cruise observations aboard R/V Xuelong (Fig. 5), the average sea surface salinity was 33.3 psu; in our work, we used this constant to calculate the corresponding freezing point, −1.83 °C. The lowest air temperature during the study period (between vertical dashed lines in Fig. 5) was approximately −5.07 °C, which is favorable for new-ice production. The air reached melting temperatures on the day of the figure (January 9, 2011), violating the conditions for the sea ice thickness retrieval from SMOS [34], [35]. We nevertheless think the SIT retrieval is correct here within its limits because the two days before, air temperature was continuously below 0 °C (Fig. 5), so that the warming should not influence strongly the SIT retrieval results. This is confirmed by comparison with the SIT maps of the preceding days which only
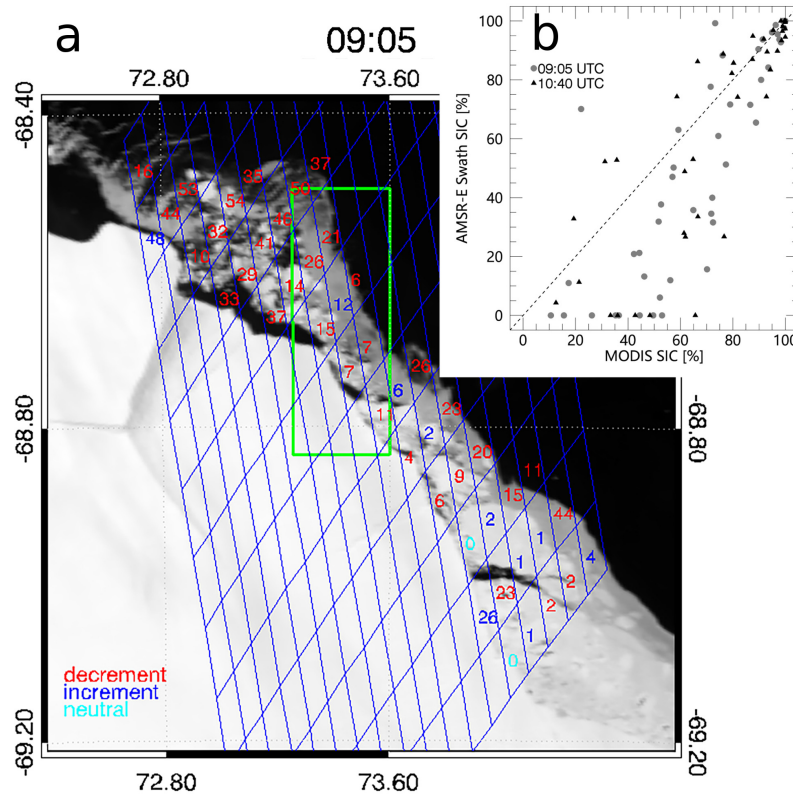
Fig. 13. (a) AMSR-E swath SIC difference with respect to MODIS-Aqua SIC at 09:05 UTC, January 9, 2011. The green rectangle outlines AMSR-E detection grid, and the blue and red numbers denote negative and positive difference (%) of AMSR-E SICs with respect to MODIS. (b) Scatterplots of AMSR-E swath SICs and MODIS-Aqua SIC at 09:05 UTC and 10:40 UTC.
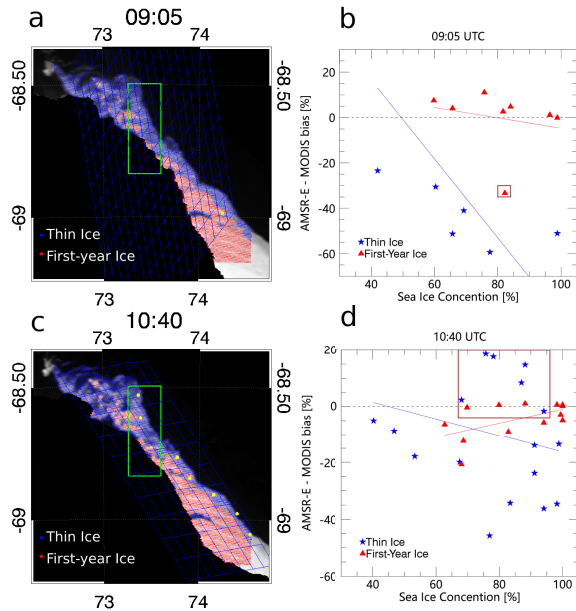

Fig. 14. Ice-type distribution based on MODIS-Aqua SIC at (a) 09:05 UTC and (c) 10:40 UTC, January 9, 2011. (The green rectangles represent the area of the aerial image.) (b) and (d) Corresponding SIC scatterplots of AMSR-E SIC biases versus thin ice and first-year ice fractions.
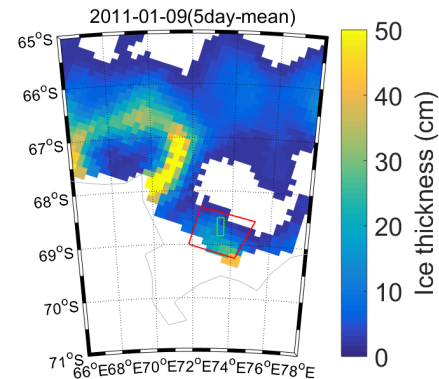

Fig. 15. Sea-ice thickness inferred from SMOS sensor observations [32], [33] from 12.5 km above study region on January 9, 2011. (The green and red quadrilaterals outline the aerial survey region and moderate-resolution-imaging spectroradiometer subimagery, respectively.).

show little change (not shown here). First-year ice is dominant, while the thin ice mainly exists in a narrow zone along the ice edge and in the northwestern part of the MODIS scene.

Over the ice-covered regions depicted in Figs. 13(b) and 15(a) and (c), there are nearly 30 AMSR-E grids for each MODIS scene. Every AMSR-E grid is color-labeled by ice type derived from the MODIS classification. The average biases between AMSR-E and MODIS results for thin ice and first-year ice are −22% and −3%, respectively (Table II), indicating significant underestimation of thin ice pixels. Furthermore, the thin ice SIC bias (−33%) mainly results from the scene depicted in Fig. 14(a), while the first-year ice bias (−5%) mainly results from the scene depicted in Fig. 14(b). Fig. 14(b) and (d) shows a more quantitative analysis of the

TABLE II
STATISTICS OF DIFFERENT SURFACE TYPE ESTIMATES (RMS)

	New ice		Young ice		First-year ice	
Author/year	bias	RMS errors	bias	RMS errors	bias	RMS errors
Wiebe et al. (2009) [17]	16.4% to 8.5%	1.2% to 4.7%	−4% to 0%	3% to 9%	−1% to 0%	1% to 4%
Cavalieri et al. (2010) [13]	−18%	24%	/	/	−3.2% to 0.4%	1.8% to 8.3%
	Thin ice				First-year ice	
This work	−22%	36%			−3%	10%

relation between the proportions of different sea-ice types calculated for every AMSR-E grid cell and considering the AMSR-E SICs bias relative to the MODIS-Aqua SICs. In general, for the grids dominated by first-year ice, the higher the concentration, the smaller the bias. For lower first-year SICs, the trend is not unique: it has positive values in Fig. 14(a) and negative values in Fig. 14(b).

The correlation between the concentration of thin ice and bias is significant in Fig. 14(b), but weak in Fig. 14(d). There are six grids [blue stars in the rectangle in Fig. 14(d)] dominated by thin ice but which have SICs similar to MODIS-Aqua, and these grids are mainly located near the edge of first-year ice [yellow dots in Fig. 14(c)]. The cause of positive SIC bias of thin ice in Fig. 14(d) (the blue stars in the brown frame) is not captured by our observations. There is only a 95-min time difference between two MODIS scenes so that not much melting or change in illumination should occur. Moreover, both Fig. 14(a) and (b) have been taken around local noon so that changes in shadows from ice structures like ridges should contribute only little to the difference. All observations related to this article have been taken in austral summer, when the ice properties are more variable than in winter. Under these conditions, the comparison of Fig. 14(b) and d shows that the retrieval of first-year ice SIC is more stable than that of thin ice.

In this article, we found the bias and rms values of the ASI algorithms to be larger than those in previously published studies, especially the bias for thin ice (Table II). Temperatures well above 0 °C in the days before the airborne observations on January 9, 2011 (Fig. 5) may have contributed to this effect. Generally, SIC retrievals from passive-microwave observations tend to be less reliable and to underestimate under melting conditions when the sea ice becomes wet, even before melt ponds start forming [19], [45]. Areas of melt pond, rare on Antarctic sea ice, should be detected as open water by both optical and passive microwave sensors and, therefore, should not contribute to the discrepancy. Also, it is probable that the surface wetness is horizontally unevenly distributed due to sea-ice deformation processes, an aspect which would explain the higher rms values that we found here in comparison to previous studies (Table II). Moreover, the surface melt in the days before the aerial observations may have reduced the albedo [46] so that the thresholds for ice-type discrimination taken from Brandt *et al.* [44] may have experienced slight

shifts. However, the values from their work are the best reference values we currently have due to the fact that no separate albedo values were taken for the different ice types under exactly the same conditions as those employed by our campaign.

V. CONCLUSION

With the widespread application of AMSR-E/AMSR2 high-resolution SIC data products, their evaluation and verification have become an important issue. In our work, we used SIC from a high-resolution aerial image obtained during China's 27th Antarctic expedition to validate ASI AMSR-E SIC products. Furthermore, we achieved a step-by-step validation of ASI SIC by using a combination of the aerial image, MODIS, and AMSR-E data. We maintain that when data from campaign experiments and satellite observations are asynchronous, the step-by-step validation method suggested here would be helpful.

In comparison with the SICs from MODIS imagery, the daily-mean ASI AMSR-E products underestimate thin ice and first-year ice by about 22% and 3%, respectively (Table II). In areas mainly covered by shelf ice or open water, AMSR-E SICs are generally consistent with those from the aerial image. But in brash-ice areas far away from the ice shelf, the ASI data underestimate the SIC. Based on the synchronicity of MODIS-Aqua and AMSR-E as well as that of MODIS-Terra and the aerial image, we have presented the successive verification of passive microwave data by remote sensing visible imageries and an aerial image in a clearly structured step-by-step method. First, we determined the tie-point values of MODIS-Terra imagery based on the aerial image. Then, in a selected region with quasimotionless ice, we assumed that MODIS-Terra and MODIS-Aqua had the same SICs and acquired tie-point values of MODIS-Aqua images and corresponding SIC values. Finally, we used this validated MODIS-Aqua SIC to assess the accuracy of AMSR-E SICs. After the step-by-step validation, it was apparent that the ASI AMSR-E product underestimates the true concentration, as is the case for other methods based on visible-imagery sensor data (Table II), and that the overall average underestimation is about 8.5% in relation to the SICs from MODIS imagery.

From our work with the ASI AMSR-E, we conclude that a higher uncertainty exists in the passive microwave SIC products of thin ice and first-year ice, for example, the rms of first-year ice (10%) is higher than rms of [13] and [17]. This higher uncertainty is due to surface melting processes before the aerial campaign, processes which decrease the reliability of passive microwave signals.

With the development of remote sensing, more and more data sources could be employed to retrieve sea ice parameters in the polar regions. In the future, more multisensors data sets could be included to evaluate sea ice parameters in a mutual way, and to improve the accuracy of sea ice products [47], [48].

REFERENCES

[1] C. L. Parkinson and D. J. Cavalieri, "Antarctic sea ice variability and trends, 1979–2010," *Cryosphere*, vol. 6, pp. 881–889, 2012, doi: 10.5194/tc6-881-2012.2012.

[2] D. J. Cavalieri and C. L. Parkinson, "Arctic sea ice variability and trends, 1979–2010," *Cryosphere*, vol. 6, no. 4, p. 881, Jul. 2012.

[3] M. Drusch, "Sea ice concentration analyses for the baltic sea and their impact on numerical weather prediction," *J. Appl. Meteorol. Climatol.*, vol. 45, no. 7, pp. 982–994, Jul. 2006.

[4] N. A. Rayner, "Global analyses of sea surface temperature, sea ice, and night marine air temperature since the late nineteenth century," *J. Geophys. Res.*, vol. 108, no. D14, 2003.

[5] D. J. Cavalieri, P. Gloersen, and W. J. Campbell, "Determination of sea ice parameters with the Nimbus 7 SMMR," *J. Geophys. Res., Atmos.*, vol. 89, no. D4, pp. 5355–5369, 1984.

[6] J. C. Comiso, "SSM/I sea ice concentrations using the bootstrap algorithm," in *National Aeronautics and Space Administration*. Annapolis, MD, USA: Goddard Space Flight Center, 1995.

[7] T. Markus and D. J. Cavalieri, "An enhancement of the NASA team sea ice algorithm," *IEEE Trans. Geosci. Remote Sens.*, vol. 38, no. 3, pp. 1387–1398, May 2000.

[8] D. M. Smith, "Extraction of winter total sea-ice concentration in the greenland and barents seas from SSM/I data," *Int. J. Remote Sens.*, vol. 17, no. 13, pp. 2625–2646, Sep. 1996.

[9] T. Lavergne *et al.*, "Version 2 of the EUMETSAT OSI SAF and ESA CCI sea-ice concentration climate data records," *Cryosphere*, vol. 13, no. 1, pp. 49–78, 2019.

[10] N. Ivanova, O. M. Johannessen, L. T. Pedersen, and R. T. Tonboe, "Retrieval of arctic sea ice parameters by satellite passive microwave sensors: A comparison of eleven sea ice concentration algorithms," *IEEE Trans. Geosci. Remote Sens.*, vol. 52, no. 11, pp. 7233–7246, Nov. 2014.

[11] J. C. Comiso, D. J. Cavalieri, C. L. Parkinson, and P. Gloersen, "Passive microwave algorithms for sea ice concentration: A comparison of two techniques," *Remote Sens. Environ.*, vol. 60, no. 3, pp. 357–384, Jun. 1997.

[12] A. Beitsch, S. Kern, and L. Kaleschke, "Comparison of SSM/I and AMSR-E sea ice concentrations with ASPeCt ship observations around antarctica," *IEEE Trans. Geosci. Remote Sens.*, vol. 53, no. 4, pp. 1985–1996, Apr. 2015.

[13] G. I. Belchansky and D. C. Douglas, "Seasonal comparisons of sea ice concentration estimates derived from SSM/I, OKEAN, and RADARSAT data," *Remote Sens. Environ.*, vol. 81, no. 1, pp. 67–81, Jul. 2002.

[14] W. N. Meier, "Comparison of passive microwave ice concentration algorithm retrievals with AVHRR imagery in arctic peripheral seas," *IEEE Trans. Geosci. Remote Sens.*, vol. 43, no. 6, pp. 1324–1337, Jun. 2005.

[15] H. Han and H.-C. Kim, "Evaluation of summer passive microwave sea ice concentrations in the chukchi sea based on KOMPSAT-5 SAR and numerical weather prediction data," *Remote Sens. Environ.*, vol. 209, pp. 343–362, May 2018.

[16] D. J. Cavalieri, T. Markus, D. K. Hall, A. J. Gasiewski, M. Klein, and A. Ivanoff, "Assessment of EOS Aqua AMSR-E arctic sea ice concentrations using Landsat-7 and airborne microwave imagery," *IEEE Trans. Geosci. Remote Sens.*, vol. 44, no. 11, pp. 3057–3069, Nov. 2006.

[17] J. F. Heinrichs, D. J. Cavalieri, and T. Markus, "Assessment of the AMSR-E sea ice-concentration product at the ice edge using RADARSAT-1 and MODIS imagery," *IEEE Trans. Geosci. Remote Sens.*, vol. 44, no. 11, pp. 3070–3080, Nov. 2006.

[18] D. J. Cavalieri, T. Markus, D. K. Hall, A. Ivanoff, and E. Glick, "Assessment of AMSR-E antarctic winter sea-ice concentrations using Aqua MODIS," *IEEE Trans. Geosci. Remote Sens.*, vol. 48, no. 9, pp. 3331–3339, Sep. 2010.

[19] G. Spreen, L. Kaleschke, and G. Heygster, "Sea ice remote sensing using AMSR-E 89-GHz channels," *J. Geophys. Res.*, vol. 113, no. C2, Feb. 2008.

[20] G. Heygster *et al.*, "AMSR-E geolocation and validation of sea ice concentrations based on 89GHz data," *J. Remote Sens. Socie. Jpn.*, vol. 29, no. 1, pp. 226–235, 2009.

[21] X. Pang, J. Pu, X. Zhao, Q. Ji, M. Qu, and Z. Cheng, "Comparison between AMSR2 sea ice concentration products and pseudo-ship observations of the arctic and antarctic sea ice edge on cloud-free days," *Remote Sens.*, vol. 10, no. 2, p. 317, 2018.

[22] X. Zhao, H. Su, A. Stein, and X. Pang, "Comparison between AMSR-E ASI sea-ice concentration product, MODIS and pseudo-ship observations of the antarctic sea-ice edge," *Ann. Glaciology*, vol. 56, no. 69, pp. 45–52, 2015.

[23] H. Wiebe, G. Heygster, and T. Markus, "Comparison of the ASI ice concentration algorithm with Landsat-7 ETM+ and SAR imagery," *IEEE Trans. Geosci. Remote Sens.*, vol. 47, no. 9, pp. 3008–3015, Sep. 2009.

[24] Y. Xi, B. Sun, and X. Li, "Assessment of AMSR-E ASI sea ice concentration using ship observations and Landsat-7 ETM+ imagery," *Yaogan Xuebao J. Remote Sens.*, vol. 17, no. 3, pp. 514–526, May 2013.

[25] J. Lu, G. Heygster, and G. Spreen, "Atmospheric correction of sea ice concentration retrieval for 89 GHz AMSR-E observations," *IEEE J. Sel. Topics Appl. Earth Observ. Remote Sens.*, vol. 11, no. 5, pp. 1442–1457, May 2018.

[26] H. M. Lam, G. Spreen, G. Heygster, C. Melsheimer, and N. W. Young, "Erroneous sea-ice concentration retrieval in the east antarctic," *Ann. Glaciology*, vol. 59, no. 76, pp. 201–212, Jul. 2018.

[27] P. Lu, Z. Li, B. Cheng, R. Lei, and R. Zhang, "Sea ice surface features in arctic summer 2008: Aerial observations," *Remote Sens. Environ.*, vol. 114, no. 4, pp. 693–699, Apr. 2010.

[28] L. Zhu, W. Wu, and Q. Lou, "Aerial imagegrammetry of antarctica? S amery ice shelf edge and GPS data solution of control point," *Geomatics Spatial Inf. Technol.*, vol. 8, p. 018, 2012.

[29] E. F. Vermote, S. Y. Kotchenova, and J. P. Ray, "MODIS surface reflectance user's guide," *MODIS Land Surf. Reflectance Sci. Comput. Facility, Version*, vol. 1, Feb. 2011.

[30] *FLAASH User's Guide, ENVI FLAASH, Version 1.0*, Research Systems, Boulder, CO, USA, 2001, pp. 8–40.

[31] H. Su and Y. Wang, "Using MODIS data to estimate sea ice thickness in the Bohai Sea (China) in the 2009–2010 winter," *J. Geophys. Res., Oceans*, vol. 117, no. C10, Oct. 2012.

[32] M. Huntemann, G. Heygster, L. Kaleschke, T. Krumpen, M. Mäkynen, and M. Drusch, "Empirical sea ice thickness retrieval during the freeze-up period from SMOS high incident angle observations," *Cryosphere*, vol. 8, no. 2, pp. 439–451, 2014.

[33] G. Spreen *et al. SMOS Sea Ice Thickness Data (Huntemann 2008)*. Institute of Environmental Physics, Univ. Bremen, Germany. Updated Daily. Accessed: Mar. 3, 2019. [Online]. Available: https://seaice.uni-bremen.de/thin-ice-thickness

[34] J. Zhang, "Meteorological datasets of cruise observation during the 27th CHINARE from 2010 to 2011," in *Data-Sharing Platform of Polar Science, Chinese Antarctic and Arctic Data Centre-CHINARE*, 2013, doi: 10.11856/sns.D.2013.014.v0.

[35] J. Kittler and J. Illingworth, "Minimum error thresholding," *Pattern Recognit.*, vol. 19, no. 1, pp. 41–47, 1986.

[36] C. Gignac, M. Bernier, K. Chokmani, and J. Poulin, "IceMap250—Automatic 250 m sea ice extent mapping using MODIS data," *Remote Sens.*, vol. 9, no. 1, p. 70, 2017.

[37] J. Su *et al.*, "The experiment and validation of sea ice concentration AMSR-E retrieval algorithm in polar region," *Yaogan Xuebao J. Remote Sens.*, vol. 17, no. 3, pp. 495–513, 2013.

[38] G. Hao and J. Su, "A study on the dynamic tie points ASI algorithm in the arctic ocean," *Acta Oceanologica Sinica*, vol. 34, no. 11, pp. 126–135, Nov. 2015.

[39] J. R. Key *et al.*, "Snow and ice products from suomi NPP VIIRS," *J. Geophys. Res., Atmos.*, vol. 118, no. 23, pp. 12816–12830, Dec. 2013.

[40] Y. Liu, J. Key, and R. Mahoney, "Sea and freshwater ice concentration from VIIRS on suomi NPP and the future JPSS satellites," *Remote Sens.*, vol. 8, no. 6, p. 523, 2016.

[41] S. Liang, A. H. Strahler, and C. Walthall, "Retrieval of land surface albedo from satellite observations: A simulation study," *J. Appl. Meteorol.*, vol. 38, no. 6, pp. 712–725, Jun. 1999.

[42] S. Ackerman, "MODIS atmosphere L2 cloud mask product," in *NASA MODIS Adaptive Processing System*. Annapolis, MD, USA: Goddard Space Flight Center, 2015.

[43] WMO (World Meteorological Organization), WMO Sea Ice Nomenclature, Terminology, Codes, and Illustrated Glossary, Secretariat World Meteor. Org., Geneva, Switzerland, 1970.

[44] R. E. Brandt, S. G. Warren, A. P. Worby, and T. C. Grenfell, "Surface albedo of the antarctic sea ice zone," *J. Climate*, vol. 18, no. 17, pp. 3606–3622, Sep. 2005, doi: 10.1175/JCLI3489.1.

[45] S. Kern, A. Rösel, L. T. Pedersen, N. Ivanova, R. Saldo, and R. T. Tonboe, "The impact of melt ponds on summertime microwave brightness temperatures and sea-ice concentrations," *Cryosphere*, vol. 10, no. 5, pp. 2217–2239, 2016.

[46] L. Istomina *et al.*, "Melt pond fraction and spectral sea ice albedo retrieval from MERIS data—Part 1: Validation against *in situ*, aerial, and ship cruise data," *Cryosphere*, vol. 9, pp. 1551–1566, Jan. 2015, doi: 10.5194/tc-9-1551-2015.

[47] R. C. Scarlat, G. Heygster, and L. T. Pedersen, "Experiences with an optimal estimation algorithm for surface and atmospheric parameter retrieval from passive microwave data in the arctic," *IEEE J. Sel. Topics Appl. Earth Observ. Remote Sens.*, vol. 10, no. 9, pp. 3934–3947, Sep. 2017.

[48] L. Kilic *et al.*, "Estimating the snow depth, the snow-ice interface temperature, and the effective temperature of Arctic sea ice using advanced microwave scanning Radiometer 2 and ice mass balance buoy data," *Cryosphere*, vol. 13, no. 4, pp. 1283–1296, 2019.

Qian Shi received the B.S. degree and the Ph.D. degree in physical oceanography from the Ocean University of China, Qingdao, China, in 2013 and 2019, respectively.

He is currently conducting post-doctoral research at Sun Yat-sen University, Guangzhou, China. His work focuses on sea ice remote sensing and the numerical simulation on Arctic sea ice. His research interests include retrieval of sea ice motion in Fram Strait and the change of sea ice outflow from the Arctic.
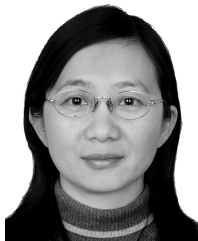
Jie Su received the B.S. degree and the Ph.D. degree in physical oceanography from the Ocean University of China, Qingdao, China, in 1988 and 2001, respectively.

Her recent study directions are sea-ice interannual and decadal variability, sea-ice model and ice-ocean coupling numerical simulation, and sea-ice remote sensing.

Georg Heygster (Member, IEEE) received the diploma and Ph.D. degrees in solid state physics with the University of Göttingen, Göttingen, Germany, in 1976 and 1979, respectively, the latter in the field of digital image processing on statistical properties of rank filters.

He worked at the Computer Center of the University of Bremen, Bremen, Germany, as a Consultant with the fields of digital image processing and nonnumerics. In 1987, he switched back to physics, first for one year to the Institute of Material Science, working on transmission properties of the Scanning Acoustic Microscope, and since 1988 to the Institute on Environmental Physics. Initially, he investigated methods to improve the resolution in maps of sea ice obtained from passive microwave radiometers. Later, he extended his field of work to remote sensing of the polar atmosphere, tropical convective systems, ice clouds, and regional satellite remote sensing tasks like topographic maps of the Wadden sea. The list of used sensors has been extended gradually to a wide range, comprising, but not limited to scatterometers, SAR and optical sensors like MODIS and MERIS. Since 2016, he has been working as a Free Consultant, mainly for the University of Bremen.

Jiuxin Shi received the B.S. degree in physical oceanography from the Ocean University of China, Qingdao, China, in 1992, and the Ph.D. degree in marine science from the Institute of Oceanology, Chinese Academy of Sciences, Beijing, China, in 2000, respectively.

His research interests include variations of water masses and circulation in the polar oceans, as well as the dynamic and thermodynamic processes in the coastal polynyas and in the cavity under ice shelves.

Lianzhong Wang received the M.S. degree in geographic information system and remote sensing from the Asian Institute of Technology, Khlong Nueng, Thailand, in 2006.

His work focuses on geodetic surveying, aerial photograph, map marking, and engineering surveying.
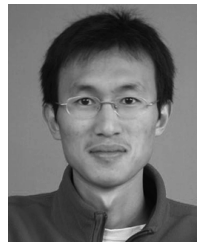
Lizhong Zhu received M.S. degree in geodesy and survey engineering from Wuhan University, Wuhan, China, in 2009.

His research interests include multisource GNSS data processing, monitoring of Antarctic ice sheet movement, and unmanned aerial vehicle photogrammetry.

Quanli Lou received the B.S. degree in aerial photography from Harbin Metallurgical Surveying School, Harbin, China, in 1983, and the M.S. degree in geodetic surveying from Wuhan University, Wuhan, China, in 2002.

His work focus in technology design for aerial photograph.

Valentin Ludwig received the B.Sc. degree in geophysics and oceanography and the M.Sc. degree in integrated climate system sciences from the University of Hamburg, Hamburg, Germany. He is currently pursuing the Ph.D. degree with the University of Bremen, Bremen, Germany.

In his Ph.D. work, he works on merging sea ice concentration data from different satellite measurements in the visible, thermal infrared, and passive microwave spectra. His research is focused on sea ice remote sensing.